Controlling of spatial modes in multi-mode photonic crystal nanobeam cavity

Fujun Sun,[1] **Yan Yang,[1]** **Zhihua Li,[1]** **Daquan Yang,[2]** **Huiping Tian,[2,4]** **and Chengkuo Lee[3,5]**

[1] *Integrated Circuit Advanced Process Center, Institute of Microelectronics, Chinese Academy of Sciences, Beijing 100029, China*
[2] *State Key Laboratory of Information Photonics and Optical Communications, Beijing University of Posts and Telecommunications, Beijing 100876, China*
[3] *Department of Electrical and Computer Engineering, National University of Singapore, 117583, Singapore*
[4] *hptian@bupt.edu.cn*
[5] *elelc@nus.edu.sg*

Abstract: We numerically and experimentally present the characteristics of disturbed spatial modes (air mode and dielectric mode) in multi-mode photonic crystal nanobeam cavity (PCNC) in the mid-infrared wavelength range. The results show that the resonance wavelength of the spatial modes can be controlled by modifying the size, period and position of the central periodical mirrors in PCNC, achieving better utilization of the spectrum resource. Additionally, side coupling characteristics of PCNC supporting both air and dielectric modes are investigated for the first time. This work serves as a proof of design method that the spatial modes can be controlled flexibly in PCNC, paving the way to achieve integrated multi-function devices in a limited spectrum range.

1. Introduction

One-dimensional (1D) photonic crystal nanobeam cavity (PCNC) is considered as an excellent platform for optical lasering [1,2], filtering [3–5], optical modulation/switching [6–9] and sensing [10–14], owing to their ultra-high quality (*Q*) factor, small mode volume (*V*) and compact size. Previously reported PCNCs were almost limited to applying the deterministic design method to achieve high *Q*-factor and low *V*, confining only dielectric modes or air modes near the band gap edges (PBGs) [15]. It is convenient to refer to the modes with resonant frequencies close to the band above and below a PBG as air modes and dielectric modes respectively based on where the energy of their modes is concentrated [16]. However, in addition to high Q-factor and low V, it has long been desired to achieve multiple resonances simultaneously for the applications such as multiple parameters sensing [17,18], multiple narrow-band light sources [19], integrated nonlinear devices [20,21], filters [22] and multifunctional devices [23]. Therefore, slow light enhanced PCNC confining different spatial modes (air and dielectric modes) simultaneously near PBGs was demonstrated in our previous study [24].

However, the free spectral range (FSR) between air and dielectric modes is limited by PBG. Usually, large PBG is needed to achieve high *Q* by enhancing the mirror strength [15]. This will induce the air and dielectric modes be separated by large spectrum range, resulting in inefficient spectrum utilization. Additionally, because PBG width is related to the refractive index contrast, to achieve a narrow PBG in a limited spectra range, the feature sizes of the unit cells should be rather small, inducing the difficulty of device fabrication. Hence, it is difficult to control and apply the two spatial modes simultaneously, efficiently and flexibly in a limited spectra range in practice [24–26]. As known, the wavelength of resonance mode is proportional to the effective refractive index which is strongly related to the geometric parameters [27,28]. Therefore, the spatial modes can be controlled by modifying the structural spatial distribution to disturb the

electric field profiles. Intuitively, due to the unique distinct field distributions of air and dielectric modes, by disturbing the low (high) refractive index regions, the air (dielectric) modes will be affected, while the dielectric (air) modes will almost keep unchanged. However, up to date, the feasibility and characteristics have never been demonstrated and explored thoroughly in PCNCs.

In this study, we numerically and experimentally analyze the characteristics of disturbed spatial modes by modifying the size, period and position of the central periodical mirrors based on our reported multi-mode PCNC [24]. We can observe the influence of structure disturbance on the resonance wavelength of air and dielectric modes simultaneously in a single cavity, achieving flexible controlling of FSR in PCNC. The results show that the FSR between fundamental spatial modes can be reduced by half through modifying the structure parameters of PCNC. Furthermore, our previously reported multi-mode PCNC uses a traditional in-line configuration to couple light into the cavity. Compared with the in-line coupling PCNC characterized by low-intensity baseline and resonance peaks, the side coupled structure characterized by a high-intensity baseline and resonance dips is easier to be measured in practice [29,30]. Therefore, here, we experimentally study the side coupling characterization of the multi-mode PCNC. Our work offers opportunities to realize multifunctional devices, paving the way to integrated light sources, filtering, biomedical sensing and environmental monitoring.
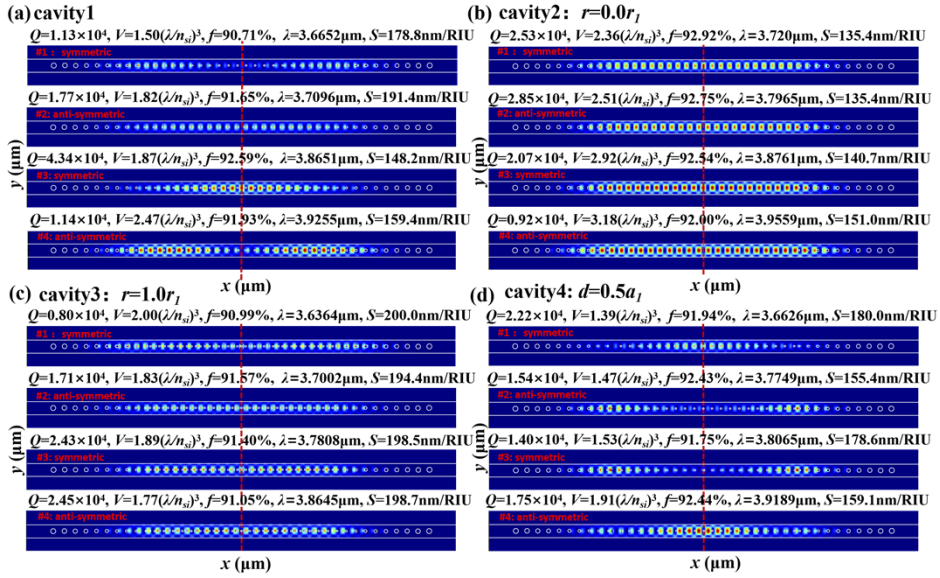
2. Design and analysis

The cavity1 shown in Fig. 1(a) is the schematic of PCNC supporting both air and dielectric modes in Ref. [24], which consists of an array of circular air holes etched into a silicon strip waveguide. The taper sections are treated as reflectors to confine both air and dielectric modes by linear tapering a and r simultaneously with a step of 20 nm from center to both sides ($a_i = a_1 + 20(i-1)$, $r_i = r_1 + 20(i-1)$, i increases from 1 to N_{taper}). The central mirror sections are designed to make the air and dielectric modes move deeper into the band edges to achieve slow light enhanced characteristics. The thickness of the nanobeam is 500nm, and the waveguide width w is chosen as 1.30μm. The central lattice constant a_1 is set as 850nm and r_1 is set as 80nm. Here, N_{taper} and N_{inner} are set as 10, respectively. Details of the design principle and method were discussed in our previous work [24].

The corresponding transmission spectra calculated by three dimensional finite difference time domain (3D-FDTD) simulation method are presented in Fig. 1(b), exhibiting PBG, fundamental (0th-order), and first-order (1st-order) spatial modes. The corresponding calculated electric energy density ($\varepsilon \cdot E^2$) profiles in the xy plane taken at the center of the silicon layer are shown in Fig. 2(a). And their separate Q-factor, mode volume V(defined as $V = \int dV \varepsilon \cdot |E|^2 / (\varepsilon \cdot |E|^2)_{max}$), confinement factor f, resonance wavelength λ and refractive index sensitivity S are marked in the picture correspondingly. As shown, due to the large percent of optical field confined in narrow space, compared with dielectric modes, smaller mode volumes for air modes are achieved. The calculated V for 0th-order air and dielectric modes in cavity1 are $1.82(\lambda/n_{si})^3$ and $1.87(\lambda/n_{si})^3$, respectively. Here, the Q-factor is evaluated by $Q = w_c U/P$, where w_c is the resonance frequency, U is the electromagnetic energy in the cavity and P is the rate of energy loss. The cavity loss is composed of the radiation loss into the free space (characterized by Q_r), absorption loss (characterized by Q_a) and the coupling loss to the feeding waveguide (Q_w). Thus, the net dimensionless decay rate $1/Q$ can be written as the sum of three decay rates: $1/Q = 1/Q_w + 1/Q_r + 1/Q_i = 1/Q_w + 1/Q_i$ [29]. Q_i is the intrinsic loss of the cavity ($Q_i = 1/Q_r + 1/Q_a$). Table 1 shows the corresponding calculated Q_w, Q_i and Q. The results indicate that the Q-factors of the resonance modes here are limited by Q_w. In further studies, the Q-factors can be improved by decreasing the waveguide coupling loss. An appropriate measure of the degree of concentration of the electricity in the high index region is defined as $f = \int_{\varepsilon(si)} dV \varepsilon \cdot |E|^2 / \int dV \varepsilon \cdot |E|^2$ [16]. For the 0th-order air and dielectric mode, 92.00% and 93.81% of electric field energy are located
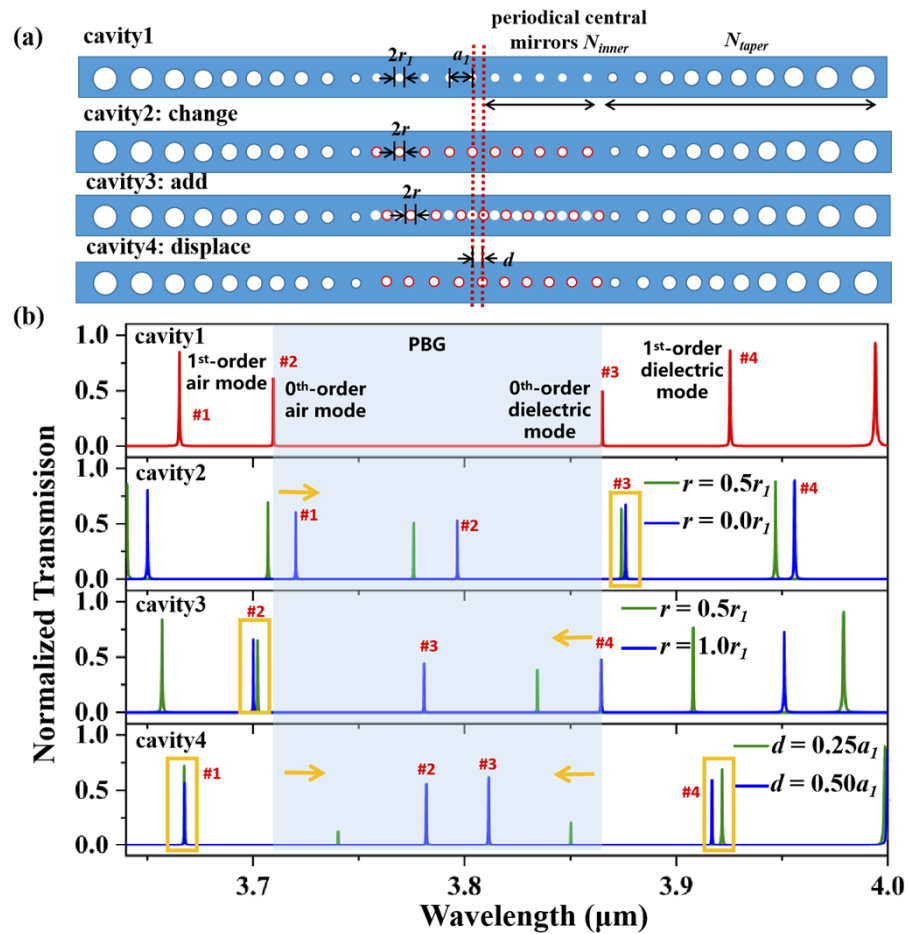
Fig. 1. (a) Schematic illustration of cavity1 and modified cavities marked as cavity2, cavity3 and cavity4. Detailed descriptions of parameters in the figures can be found in the main text. For the taper section, both lattice constant and radius are linearly modulated from the center to both sides. For the inner section in cavity1, the lattice constant and radius are kept as constant as a_1 and r_1, respectively. For cavity2, the radius of central mirrors is adjusted to r. For cavity 3, at the position of half lattice, holes with radius r are added. For cavity4, central mirrors are displaced along x-direction with distance d. (b) Corresponding calculated transmission spectra. The yellow frames indicate the modes which are robust against the structural modification. The arrows indicate the moving tendency of the disturbed spatial modes.

in silicon respectively, which indicates the different electrical field distributions. Based on the perturbation theory, the S is related with the resonance wavelength and confinement factor in air [24]. Here, to demonstrate the different response of air and dielectric modes to external environmental change, the sensing performance of the resonance modes are shown. By varying the environmental refractive index, the S of 191.4 nm/RIU and 148.2 nm/RIU calculated by $S = \Delta\lambda/\Delta n$ are achieved ($\Delta\lambda$ the wavelength shift, Δn the change of refractive index) for 0th-order air and dielectric modes, respectively. Additionally, the FSR between 0th-order air and dielectric modes of cavity1 is ~155.5nm, resulting in a waste of spectrum resources. Therefore, to better utilize the spectrum resource, the spatial modes should be controlled flexibly to achieve smaller FSR by modifying the spatial distributions and sizes of air holes in the central mirrors.

(a) cavity1
$Q=1.13\times10^4$, $V=1.50(\lambda/n_{si})^3$, $f=90.71\%$, $\lambda=3.6652\mu m$, $S=178.8nm/RIU$

$Q=1.77\times10^4$, $V=1.82(\lambda/n_{si})^3$, $f=91.65\%$, $\lambda=3.7096\mu m$, $S=191.4nm/RIU$

$Q=4.34\times10^4$, $V=1.87(\lambda/n_{si})^3$, $f=92.59\%$, $\lambda=3.8651\mu m$, $S=148.2nm/RIU$

$Q=1.14\times10^4$, $V=2.47(\lambda/n_{si})^3$, $f=91.93\%$, $\lambda=3.9255\mu m$, $S=159.4nm/RIU$

(b) cavity2: $r=0.0r_1$
$Q=2.53\times10^4$, $V=2.36(\lambda/n_{si})^3$, $f=92.92\%$, $\lambda=3.720\mu m$, $S=135.4nm/RIU$

$Q=2.85\times10^4$, $V=2.51(\lambda/n_{si})^3$, $f=92.75\%$, $\lambda=3.7965\mu m$, $S=135.4nm/RIU$

$Q=2.07\times10^4$, $V=2.92(\lambda/n_{si})^3$, $f=92.54\%$, $\lambda=3.8761\mu m$, $S=140.7nm/RIU$

$Q=0.92\times10^4$, $V=3.18(\lambda/n_{si})^3$, $f=92.00\%$, $\lambda=3.9559\mu m$, $S=151.0nm/RIU$

(c) cavity3: $r=1.0r_1$
$Q=0.80\times10^4$, $V=2.00(\lambda/n_{si})^3$, $f=90.99\%$, $\lambda=3.6364\mu m$, $S=200.0nm/RIU$

$Q=1.71\times10^4$, $V=1.83(\lambda/n_{si})^3$, $f=91.57\%$, $\lambda=3.7002\mu m$, $S=194.4nm/RIU$

$Q=2.43\times10^4$, $V=1.89(\lambda/n_{si})^3$, $f=91.40\%$, $\lambda=3.7808\mu m$, $S=198.5nm/RIU$

$Q=2.45\times10^4$, $V=1.77(\lambda/n_{si})^3$, $f=91.05\%$, $\lambda=3.8645\mu m$, $S=198.7nm/RIU$

(d) cavity4: $d=0.5a_1$
$Q=2.22\times10^4$, $V=1.39(\lambda/n_{si})^3$, $f=91.94\%$, $\lambda=3.6626\mu m$, $S=180.0nm/RIU$

$Q=1.54\times10^4$, $V=1.47(\lambda/n_{si})^3$, $f=92.43\%$, $\lambda=3.7749\mu m$, $S=155.4nm/RIU$

$Q=1.40\times10^4$, $V=1.53(\lambda/n_{si})^3$, $f=91.75\%$, $\lambda=3.8065\mu m$, $S=178.6nm/RIU$

$Q=1.75\times10^4$, $V=1.91(\lambda/n_{si})^3$, $f=92.44\%$, $\lambda=3.9189\mu m$, $S=159.1nm/RIU$

Fig. 2. Calculated energy density distributions in xy plane for resonance modes in (a) cavity1, (b) cavity2, (c) cavity3, and (d) cavity4 shown in Fig. 1(b). Q-factors, mode volume V, confinement factor f, resonance wavelength λ, refractive index sensitivity S, and symmetries of the modes are indicated in the plot. The symmetry plane is indicated by the red dashed line.

Table 1. Calculated Q_w, Q_i, and Q of the resonance modes

Modes	Cavity1				Cavity2				Cavity3				Cavity4			
	#1	#2	#3	#4	#1	#2	#3	#4	#1	#2	#3	#4	#1	#2	#3	#4
$Q_w(\times10^4)$	1.15	1.82	4.45	1.16	2.69	2.97	2.11	0.93	0.84	1.80	2.96	2.70	2.34	1.71	1.59	1.86
$Q_i(\times10^5)$	6.14	6.86	18.26	9.85	4.44	7.52	12.26	9.60	1.50	3.64	1.37	2.63	4.45	1.56	1.17	3.03
$Q(\times10^4)$	1.13	1.77	4.34	1.14	2.53	2.85	2.07	0.92	0.80	1.71	2.43	2.45	2.22	1.54	1.40	1.75

Schematics of the modified structures are shown in Fig. 1(a), marked as cavity2, cavity3 and cavity4, respectively. With the method of modifying the central mirrors, novel photonic crystal waveguide-based cavities are presented. As expected, with the disturbance of mirror holes, modes move into the PBG, achieving controllable wavelength of spatial modes. In the following, to understand the phenomenon, numerical analyses of transmission spectra and electric density profiles are carried out to evaluate the influence of structure modulations on the Q-factor, FSR, f, V, S and λ of the multi-mode. Figure 1(b) shows the corresponding calculated transmission spectra using 3D-FDTD.

For cavity2, the air hole radius of central mirrors r_1 are modulated. We can expect that the 0th-order dielectric mode will almost keep unchanged due to the undisturbed field distribution region. While, for air modes, the field localization region is replaced by high refractive index material. Therefore, the air modes will be disturbed, moving towards longer wavelength as defect modes. The calculated transmission is shown in Fig. 1(b) and electric energy density profiles of modes #1-#4 with $r=0r_1$ shown in Fig. 2(b) correspond well with our exception. As shown, the energy spatial distributions of modes #2 and #3 are similar to that of 0th-order air and dielectric modes in cavity1. While, according to the number of nodes in electric fields, modes #1 and #4 can be hardly treated as 1st-order modes. When the radius of central mirrors is reduced to $0r_1$,

mode #3 has a slightly redshift due to the small perturbation. The calculated fraction of mode energy inside the silicon medium for mode #3 at wavelength of 3.8761µm is ~92.54%, which is similar to that of 0th-order dielectric mode in cavity1 (92.59%). According to the calculated partial Q-factors shown in Table. 1, the Q-factor of mode #3 is decreased due to the increased coupling loss to the waveguide caused by the removal of central mirrors. Mode #1 and mode #2 move towards inner PBG with the decrease of r. And compared with air modes in cavity1, both Q and V values are increased for modes #1 and #2 in cavity2. Compared with modes #1 and #2, mode #4 also has redshift, but the amount is much slighter. This can be explained by the calculated confinement factors. The calculated confinement factors of modes #1, #2 and #4 are ~92.92%, ~92.75% and ~92.00%, respectively. For dielectric modes, the values are almost keep unchanged, while, for air modes, the increments are significant. Similarly, for modes #1 and #2, the f variations also induce the decrease of S compared with the air modes in cavity1. Additionally, the FSR between modes #2 and #3 is ~79.6 nm when $r = 0.0r_1$.

For cavity3, air holes with radius r are added at the positions of half periods, making the fields of the dielectric modes confined in the low refractive index region. Therefore, compared with cavity2, the moving tendency of the spatial modes are opposite. As shown in Fig. 1(b), by adding air holes with radius $0.5r$ and $1.0r$, the resonance wavelength of mode #2 almost keeps unchanged. While, the disturbed dielectric modes #3 and #4 move into the PBG with the increase of r, due to the decrease of effective refractive index. The principle and analysis are similar to cavity2. Due to the increase of field confinement in air holes, the refractive index sensitivities for modes #1–4 in cavity3 are comparable with mode #2 in cavity1. The calculated confinement factors of modes #1, #2, #3 and #4 are ~90.99%, ~91.57%, ~91.40% and ~91.05%, respectively. As expected, for modes #3 and #4, the confinement in low refractive index is increased compared with the dielectric modes in cavity1. While, for mode #2, the calculated result almost keeps stable compared with the fundamental air mode. The FSR between modes #2 and #3 is ~80.6 nm when $r = 1.0r_1$.

For cavity4, the air hole positions of central mirrors are modulated by shifting by a distance (d) along x-direction from the original lattice position. As shown in Fig. 1(b), displacing $0.25a_1$ and $0.5a_1$ provide a small influence on the resonance wavelength of modes #1 and #4, showing robustness against the structural modification. According to the energy density distributions, for cavity4, modes #1 (symmetric) and #4 (anti-symmetric) are the 0th-order air and dielectric modes, respectively. While, for cavity1, 0th-order air mode (mode #2) and dielectric mode (mode #3) are anti-symmetric and symmetric modes, respectively. Therefore, the symmetrical properties of 0th-order air and dielectric modes in cavity1 and cavity4 are opposite. In addition, according to the number of nodes in energy density profiles, mode #2 and mode #3 are the 1st-order air and dielectric modes, respectively. Modes #2 and #3 appearing in PBG move towards each other with the increase of d. As shown, the shifting distance may increase transmission loss obviously when the distribution of holes breaks the balance of multiple interferences. The FSR between modes #2 and #3 is ~31.6nm when $d = 0.5a_1$.

3. Fabrication and results

The devices were fabricated from SOI wafers with a 500nm thick Si device layer and 2µm thick buried oxide. Electron beam lithography (JEOL JBX-6300-100kV) was performed using ZEP 520A resist spun at 6000rpm. The beam current we choose was 5nA, and an exposure dose of 300µC/cm^2 was used. The resist is developed with n-Amyl acetate developer and rinsed with IPA/MIBK. Reactive ion etching of the exposed Si regions was performed with C_4F_8, SF_6 and Ar process gases. The light is coupled into the bus waveguide by the TE subwavelength grating (SWG) coupler, then passes through the PCNC, and finally gets directed out by the other grating coupler. The measurements were performed using a linearly polarized continuous wave tunable MIR laser (3.64–4.00µm) and detector.

Usually, the in-line waveguide direct coupling PCNC has low transmission in experiments due to the large mirror strength of the high Q cavity and fabrication errors, which is rather hard to be measured. While, for the side-coupling scheme, because the light that is not resonant in the PCNC is transmitted through the side-coupler, the transmission spectrum is characterized by a high-intensity baseline and resonance dips. While, for our investigated PCNC supporting both air and dielectric modes, the characteristics of the coupled air and dielectric modes under parallel straight waveguide coupling and arc waveguide coupling conditions have not yet been investigated. Therefore, in the following, we experimentally study the PCNC from two aspects, one is the side coupling characteristics, the other is the controlling of spatial modes by modifying the central periodical mirrors.

3.1. Coupling

Firstly, we compare the in-line coupling cavity1 and two side coupling configurations (parallel straight waveguide and arc waveguide coupling) that enable evanescent coupling of light from the side coupling waveguide into the PCNC. Figure 3 shows the scanning electron microscopy (SEM) images (top image, *xy* plane) of the fabricated PCNCs with different coupling configurations, and the corresponding measured transmission spectra for cavity1 normalized to the strip waveguide structure. The coupling gap is set as 200nm. And for the arc-coupling structure, the radius of the *S* bends is 10 μm.
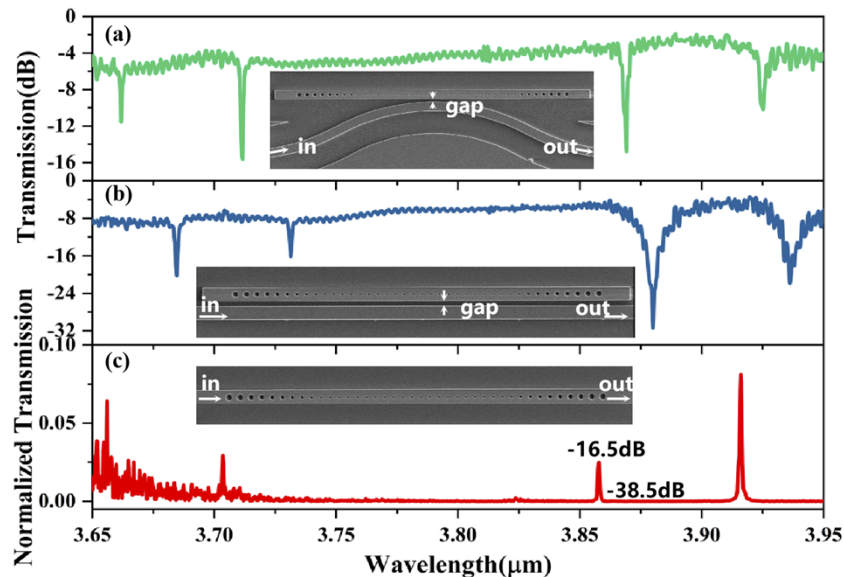
Fig. 3. Measured transmission spectra of the (a) in-line coupling, (b) parallel straight waveguide coupling and (c) arc waveguide coupling PCNC (cavity 1), and the corresponding SEM images.

For the in-line coupling cavity1, the experimental fundamental air and dielectric modes exhibit Q-factor of 5592 and 4302 at resonant wavelength of ~3.7035μm and 3.8677μm, respectively, obtained by fitting to a Lorentz profile. The insertion losses for both modes are ~16 dB. The fabrication-induced difference and random roughness (such as imperfect circular holes, rough sidewall and lag effect) are possibly the reason for the discrepancy between the fabrication batches with Ref. [24]. For direct waveguide side-coupling, the measured resonant wavelengths show significant red-shift compared with the in-line direct coupling results. Such discrepancies are mainly attributed to the fabrication-induced lag effect due to the narrow coupling gap. The

insertion loss is about 9dB at wavelength of 3.8μm. The ER for dielectric mode is ~25dB, while for air mode, it is ~8dB. Compared with the side-coupled 0th-order air mode, with the coupling gap of 200nm, the coupled 0th-order dielectric mode achieves lower measured Q and higher ER. With the increase of gap, the Q-factor of dielectric mode will increase, while air mode may be disappearing. This is because the radiation loss is much larger for air mode compared with dielectric mode caused by side-coupling with a parallel straight feeding waveguide. Thus an optimized side-coupling manner is indispensable to keep high Q-factors with high ERs for both modes.

Compared with the experimental results shown in Fig. 3(b) and (c), Fig. 3(a) illustrates the advantages of the bend side-coupled PCNC design. The experimental Q-factors of 1963 and 1447 are achieved at the resonance wavelength of about 3.711μm and 3.868μm by Lorentz fitting for 0th-order air and dielectric modes. Compared with in-line coupling, the measured Q-factors are decreased due to the increased coupling loss. The insertion loss is ~5 dB at wavelength of 3.8μm, which is lower than the parallel straight waveguide coupling and direct in-line coupling. This will make the measurement easier. Compared with the reported side coupled nanobeam cavities in the near-infrared wavelength range [28–30], here the relatively large insertion loss is likely due to the three reasons: (1) material absorption of the SiO_2 substrate, (2) scattering loss because of fabrication imperfection, and (3) contamination of the waveguide surface. The ERs for both modes are similar ~11dB. This is because the incident light must traverse the entire PCNC, including all of the mirror segments, before a transmission measurement can be made using the parallel side-coupled configuration. While, in the bend side-coupled configuration, the transmission intensity does not suffer from increased mirror strength, since light is coupled directly into and out of the central cavity region of the nanobeam. Besides, the measured FSR between the 0th-order air and dielectric modes is ~150 nm, which corresponds well with the simulation result in Fig. 1(b). We expect that the investigated structures here can be further exploited in application toward highly efficient coupling between other types of advanced photonic devices.

3.2.   Modifying of cavities

To further demonstrate the characteristics of spatial modes in PCNCs shown in Fig. 1(b), normal PCNC (cavity1) and the PCNCs with removed, doubled and shifted central periodical mirror holes (cavity2, 3 and 4) with arc feeding waveguide side-coupling structures are fabricated as shown in Fig. 4(a). The corresponding measured transmission spectra are shown in Fig. 4(b). Note that to achieve high ER defined by the ratio between the on- and off-resonance transmission, the coupling gaps for all PCNCs here are set as 200nm. As expected, the moving tendency of the resonance modes corresponds well with the calculated results shown in Fig. 1(b). As shown in Fig. 4(b), there are multiple resonator dips in the wavelength range of 3.65 to 3.95μm. And PBG is displayed in the transmission spectra of cavity1. While, for cavity2, 3 and 4 with disturbed central mirrors, spatial modes localized near PBG edges will be disturbed, moving into PBG. Lorentz fittings of the resonance modes are performed to reveal the measured resonance wavelengths, ER and Q.

With the removal of central mirrors (cavity2), the resonance wavelength of fundamental dielectric mode #3 almost keeps unchanged, achieving experimental Q-factor of 1717 at the resonance wavelength of ~3.870μm. For mode #2 arising in PBG at the resonance wavelength of ~3.796μm, measured Q-factor of 2472 is obtained. The achieved Q-factors are higher than the fundamental air and dielectric modes in cavity1. And the insertion losses for modes #2 and #3 are ~8.8 dB and 9.9 dB, respectively. The experimental FSR between these two modes is ~74 nm. With the double periodical central mirrors (cavity3), the wavelength of fundamental air mode #2 has a slightly blue shift compared with the simulation results due to the fabrication errors. Experimental Q-factor of 2203 is achieved at the resonance wavelength of ~3.773μm. While, for
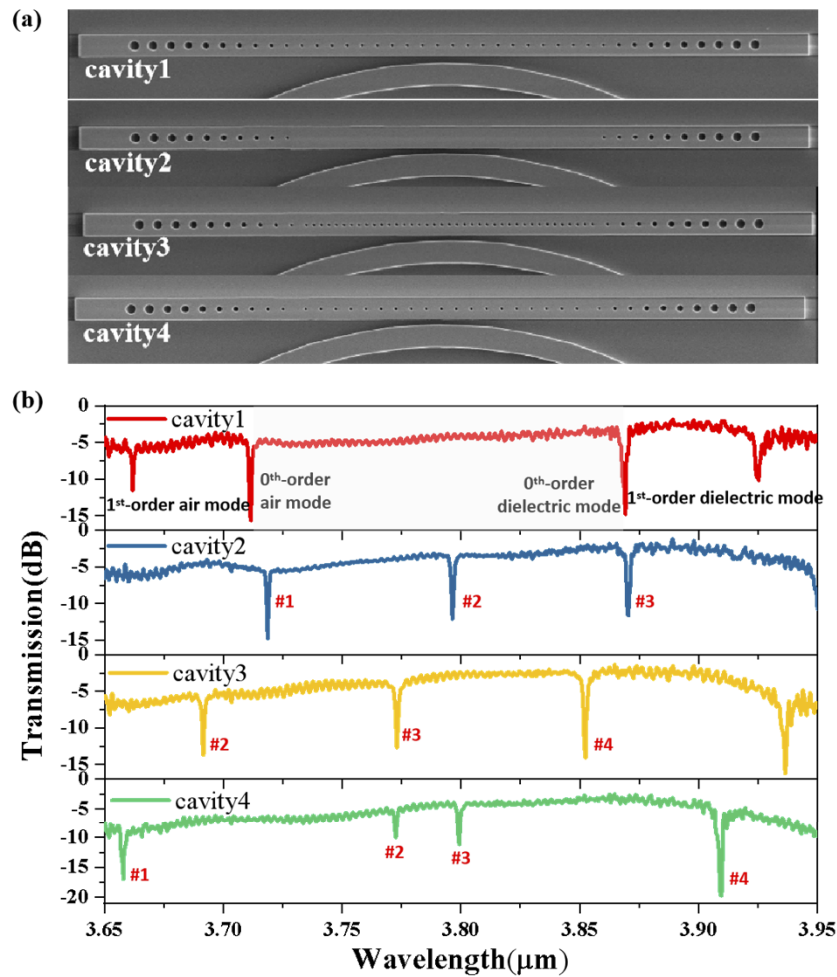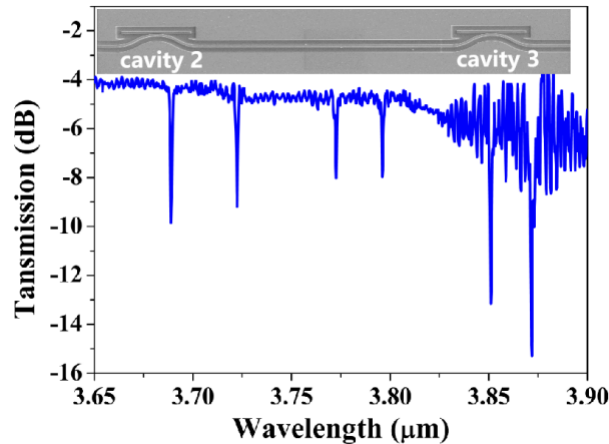
Fig. 4. (a) SEM images of the fabricated structures for cavity1, cavity2 with $r = 0.0r_1$, cavity3 with $r = 1.0r_1$ and cavity4 with $d = 0.5a_1$. (b) Measured transmission spectra.

mode #3 arising in PBG at the resonance wavelength of ~3.852μm, higher experimental Q-factor of 3439 is achieved. And the insertion losses for modes #2 and #3 are ~8.5 dB and 8.8 dB, respectively. The FSR between these two modes is ~79 nm. With the half period shift of the central mirrors (cavity4), both fundamental air mode #1 and dielectric mode #4 move away from the PBG. And higher-order modes #2 and #3 arise in PBG. The experimental Q-factors of 3698 and 3122 are achieved at the resonance wavelength of ~3.773μm and 3.799μm for higher-order air and dielectric modes, respectively. And the insertion losses for air and dielectric modes are ~5.2 dB and 7.2 dB, respectively. The FSR between these two modes is ~27 nm.

According to the analysis of the experimental results, we find that the experimental results correspond well with the simulation results, and the defect modes showing in PBG introduced by the modifying of central mirrors achieve higher Q-factor compared with the modes confined around PBG edges. Controlling method to modify both fundamental air and dielectric modes simultaneously or independently with determined resonance wavelengths and high Q-factors is demonstrated, achieving flexible controlling of FSR in PCNC. On this basis, cascaded side coupled cavities can be used to further increase the spectra information and utilization. For

instance, cavity2 and cavity3 as illustrative example of the proposed flexible approach is shown in Fig. 5. As expected, six separated resonances (modes #1, #2, #3 in cavity2 and modes #2, #3, #4 in cavity3) at different wavelength are observed which correspond well with the resonance modes in a fabricated single cavity. Additionally, for modes in cavity2, the main located position of field distributions are high dielectric material. While for caivty3, they are mainly located in the low refractive index region. Therefore, due to the distribution differences and multi-mode, the combined structure can be applied as multi-function device with high accuracy, such as sensing and lasing.

Fig. 5. Measured transmission spectra and SEM image of the fabricated cascaded structure of cavity2 and cavity3.

4. Conclusion

In conclusion, we mainly study the controlling of spatial modes in PCNC by modifying the size, period and position of central periodical mirrors to realize efficient spectrum utilization. Based on the simulation and experimental results, the wavelength of spatial modes can be controlled flexibly with high Q-factor and ER. Additionally, the experimental results show that the insertion loss of the spatial modes for in-line coupling, parallel coupling and arc coupling are 15dB, 9dB and 5dB, respectively, showing the advantage of arc waveguide side coupling. We expect that investigated engineering method can be further exploited to improve spectral utilization for application toward multi-function devices based on integrated PCNCs.

Disclosures. The authors declare no conflicts of interest.

Data Availability. Data underlying the results presented in this paper are not publicly available at this time but may be obtained from the authors upon reasonable request.

References

1. Y. Zhang, M. Khan, Y. Huang, J. Ryou, P. Deotare, R. Dupuis, and M. Lončar, "Photonic crystal nanobeam lasers," Appl. Phys. Lett. **97**(5), 051104 (2010).
2. W. Fegadolli, J. Oliveira, V. Almeida, and A. Scherer, "Compact and low power consumption tunable photonic crystal nanobeam cavity," Opt. Express **21**(3), 3861–3871 (2013).
3. P. Deotare, L. Kogos, I. Bulu, and M. Lončar, "Photonic crystal nanobeam cavities for tunable filter and router applications," IEEE J. Select. Topics Quantum Electron. **19**(2), 3600210 (2013).
4. X. Ge, Y. Shi, and S. He, "Ultra-compact channel drop filter based on photonic crystal nanobeam cavities utilizing a resonant tunneling effect," Opt. Lett. **39**(24), 6973–6976 (2014).

5. Z. Cheng, Y. Zhao, J. Zhang, H. Zhou, D. Gao, J. Dong, and X. Zhang, "Generalized Modular Spectrometers Combining a Compact Nanobeam Microcavity and Computational Reconstruction," ACS Photonics **9**(1), 74–81 (2022).

6. T. Pan, C. Qiu, J. Wu, X. Jiang, B. Liu, Y. Yang, and Y. Su, "Analysis of an electro-optic modulator based on a graphene-silicon hybrid 1D photonic crystal nanobeam cavity," Opt. Express **23**(18), 23357–23364 (2015).

7. X. Li, X. Liu, Y. Qin, D. Yang, and Y. Ji, "Ultra-Low Index-Contrast Polymeric Photonic Crystal Nanobeam Electro-Optic Modulator," IEEE Photonics J. **12**(3), 1–8 (2020).

8. H. Zhou, C. Qiu, X. Jiang, Q. Zhu, Y. He, Y. Zhang, Y. Su, and A. R. Soref, "Compact, submilliwatt, 2× 2 silicon thermo-optic switch based on photonic crystal nanobeam cavities," Photonics Res. **5**(2), 108–112 (2017).

9. Z. Meng, C. Chen, and F. Qin, "Theoretical investigation of integratable photonic crystal nanobeam all-optical switching with ultrafast response and ultralow switching energy," J. Phys. D: Appl. Phys. **53**(20), 205105 (2020).

10. P. Xu, K. Yao, J. Zheng, X. Guan, and Y. Shi, "Slotted photonic crystal nanobeam cavity with parabolic modulated width stack for refractive index sensing," Opt. Express **21**(22), 26908–26913 (2013).

11. Y. Chen, W. S. Fegadolli, W. M. Jones, A. Scherer, and M. Li, "Ultrasensitive gas-phase chemical sensing based on functionalized photonic crystal nanobeam cavities," ACS Nano **8**(1), 522–527 (2014).

12. W. Fegadolli, N. Pavarelli, P. Brien, S. Njoroge, V. Almeida, and A. Scherer, "Thermally controllable silicon photonic crystal nanobeam cavity without surface cladding for sensing applications," ACS Photonics **2**(4), 470–474 (2015).

13. Q. Qiao, J. Xia, C. Lee, and G. Zhou, "Applications of Photonic Crystal Nanobeam Cavities for Sensing," Micromachines **9**(11), 541 (2018).

14. D. Yang, X. Liu, X. Li, B. Duan, A. Wang, and Y. Xiao, "Photoic crystal nanobeam cavity devices for on-chip integrated silicon photonics," J. Semicond. **42**(2), 023103 (2021).

15. Q. Quan and M. Loncar, "Deterministic design of wavelength scale, ultra-high Q photonic crystal nanobeam cavities," Opt. Express **19**(19), 18529–18542 (2011).

16. J. D. Joannopoulos, S. G. Johnson, J. N. Winn, and R. D. Meade, *Photonic Crystals: Molding the Flow of Light* (Princeton University, 2011).

17. P. Liu and Y. Shi, "Simultaneous measurement of refractive index and temperature using cascaded side-coupled photonic crystal nanobeam cavities," Opt. Express **25**(23), 28398–28406 (2017).

18. C. Wang, Z. Fu, F. Sun, J. Zhou, and H. Tian, "Large-dynamic-range dual-parameter sensor using broad FSR multimode photonic crystal nanobeam cavity," IEEE Photonics J. **10**(5), 1–14 (2018).

19. F. Pyatkov, V. Fütterling, S. Khasminskaya, B. S. Flavel, F. Hennrich, M. M. Kappes, R. Krupke, and W. H. P. Pernice, "Cavity-enhanced light emission from electrically driven carbon nanotubes," Nat. Photonics **10**(6), 420–427 (2016).

20. Z. Tu, J. Zhang, C. Alonso-Ramos, X. Roux, L. Vivien, and E. Cassan, "Doubly resonant distributed feedback cavity with controllable wide wavelength separation.," Opt. Commun. **494**, 127064 (2021).

21. S. Buckley, M. Radulaski, J. L. Zhang, J. Petykiewicz, K. Biermann, and J. V. čkovíc, "Multimode nanobeam cavities for nonlinear optics: high quality resonances separated by an octave," Opt. Express **22**(22), 26498–26509 (2014).

22. P. Yu, H. Qiu, R. Cheng, L. Chrostowski, and J. Yang, "High-Q antisymmetric multimode nanobeam photonic crystal cavities in silicon waveguides," Opt. Express **26**(20), 26196–26204 (2018).

23. D. Sell, J. Yang, S. Doshay, R. Yang, and J. A. Fan, "Large-angle, multifunctional metagratings based on freeform multimode geometries," Nano Lett. **17**(6), 3752–3757 (2017).

24. F. Sun, J. Wei, B. Dong, Y. Ma, Y. Chang, H. Tian, and C. Lee, "Coexistence of air and dielectric modes in single nanocavity," Opt. Express **27**(10), 14085–14098 (2019).

25. F. Sun, B. Dong, J. Wei, Y. Ma, H. Tian and, and C. Lee, "Demonstration of mid-infrared slow light one-dimensional photonic crystal ring resonator with high-order photonic bandgap," Opt. Express **28**(21), 30736–30747 (2020).

26. D. Urbonas, A. Balčytis, K. Vaškevičius, M. Gabalis, and R. Petruškevičius, "Air and dielectric bands photonic crystal microring resonator for refractive index sensing," Opt. Lett. **41**(15), 3655–3658 (2016).

27. G. Kaur and H. Wanare, "Controlling spatial mode superposition to channel light flow in a photonic crystal," J. Opt. Soc. Am. B **37**(12), 3809–3818 (2020).

28. M. Lončar, J. Vučković, and A. Scherer, "Methods for controlling positions of guided modes of photonic-crystal waveguides," J. Opt. Soc. Am. B **18**(9), 1362–1368 (2001).

29. P. Yu, H. Qiu, H. Yu, F. Wu, Z. Wang, X. Jiang, and J. Yang, "High-Q and High-Order Side-Coupled Air-Mode Nanobeam Photonic Crystal Cavities in Silicon," IEEE Photonics Technol. Lett. **28**(20), 1 (2016).

30. S. Halimi, S. Hu, F. Afzal, and S. Weiss, "Realizing high transmission intensity in photonic crystal nanobeams using a side-coupling waveguide," Opt. Lett. **43**(17), 4260–4263 (2018).